Novel B19′ strain glass with large recoverable strain

Qianglong Liang, Dong Wang, Jian Zhang, Yuanchao Ji, Xiangdong Ding, Yu Wang, Xiaobing Ren, and Yunzhi Wang

Phys. Rev. Materials **1**, 033608 — Published 22 August 2017

DOI: 10.1103/PhysRevMaterials.1.033608

Novel B19′ Strain Glass with Large Recoverable Strain

Qianglong Liang[1], Dong Wang[1], Jian Zhang[1]*, Yuanchao Ji[1], Xiangdong Ding[1], Yu Wang[1], Xiaobing Ren[1,3], Yunzhi Wang[1,2]**

1. *Center of microstructure science, Frontier Institute of Science and Technology, State Key Laboratory for Mechanical Behavior of Materials, Xi'an Jiaotong University, Xi'an 710049, China.*
2. *Department of Materials Science and Engineering, The Ohio State University, 2041 College Road, Columbus, OH 43210, USA*
3. *Ferroic Physics Group, National Institute for Materials Science, Tsukuba, 305-0047, Ibaraki, Japan.*

We report for the first time a new strain glass state (B19′ strain glass) in a Ni-rich TiNi shape memory alloy produced by cold rolling. As compared to previously reported strain glasses, this new strain glass state has outstanding properties including quasi-linear superelasticity with a large recoverable strain (~4%), slim hysteresis and high strength (~1.0GPa) over a wide temperature range (~200K). The existence of the B19′ strain glass state is confirmed by (i) frequency dispersion of storage modulus, (ii) continuous decrease of electrical resistivity and (iii) continuous growth of B19′ nanodomains upon cooling. This study proves that the effect of defect strength on the creation of a strain glass state is in parallel to the effect of cooling rate on the creation of a structural glass, e.g., any strain crystal (i.e., martensite) can be turned into a strain glass if strong enough defects could be engineered.

PACS: 64.70.P-, 64.70.Nd, 81.30Kf, 62.20.fg

*Corresponding authors: Wang_dong1223@xjtu.edu.cn
Jian.zhang@xjtu.edu.cn
Wang.363@osu.edu

Since their discovery, shape memory alloys (SMAs) have enabled many critical applications [1-4] owing to their shape memory effect (SME) and superelasticity (SE). Both effects originate from a diffusionless martensitic transformation (MT) [5-10]. Since MT is a typical first-order transition, the large temperature- or stress-hysteresis and narrow temperature range of operation have severely limited the current generation of SMAs for applications that require high sensitivity, precision, durability, and energy efficiency in complex environments. Extensive efforts have been made recently to overcome these shortcomings through various means including nano-grain [11,12], nanocomposite [13], structural anisotropy [14,15], and crystallographic compatibility [16,17]. The successfulness of these approaches has been demonstrated in limited SMAs respectively.

In the past decade, both simulation and experimental studies have shown that a sharp first-order MT can be turned into a strain glass transition through defect engineering [18-29]. A strain glass transition is a new type of ferroic glass transition and the transition product, the strain glass state, consists of nanodomains of transformation strains without any long-range orders, which are parallel to relaxors [30-33] and cluster spin glasses [34-36]. During a strain glass transition, the formation of a long-range ordered, internally twinned martensitic domain state (e.g., strain crystal) is prohibited by densely populated stress-carrying defects [19]. The strain glass transition is found to have unique transition behavior, including disappearance of transition heat, frequency dispersion of modulus, no average structure change , and is accompanied by many novel properties such as quasi-linear elasticity with slim hysteresis [37], low and tunable elastic modulus [38], and Invar/Elinvar anomalies [27,39].

However, all strain glasses reported so far, including TiNi (with excess Ni) [18], TiNiX (X= Fe, Co, Cr, Mn) [21,22], TiPdX (X = Fe, Co, Cr, Mn) [23], AuCuAl [26], and the Gum metals [27], TiNi with nano precipitates [28], and TiNiFe with dislocations [29], have rather limited recoverable strains (up to 2%) and, thus, are unattractive for practical applications. Similar to MT, the recoverable strain of a strain

glass during loading is related directly to the stress-free transformation strain (SFTS). The Fe-doped TiNiFe strain glass [37] or precipitate-induced TiNi strain glass [40] consists of R martensite nanodomains and its quasi-linear superelasticity has a relatively small recoverable strain (~0.5%) because of the small SFTS of the B2 to R transition. The R strain glass can transfer into B19' martensite at higher stress with large hysteresis [40]. The oxygen-doped glassy state in TiNb [41] is an O (orthorhombic) strain glass that has also a limited recoverable strain (~2%).

The martensitic phase in the commercial NiTi SMAs is B19′ (monoclinic) and the B2 (cubic) to B19′ transition has a large transformation strain (~10%). Thus if a B19′ strain glass state could be created, much larger recoverable strains are expected. According to a recent simulation study [42], however, a large SFTS is accompanied by strong elastic interactions, making the formation of strain glass through point defect doping difficult. Lloveras et al. [43] have shown that a decrease in elastic anisotropy (strength of long-range interactions accompanying the MT) and/or increase in disorder (strength of random defects) are essential for hysteresis reduction. Thus, extended defects such as dislocations and coherent precipitates that are much "stronger" than point defects become the necessary means for the creation of strain glasses with large SFTS. Cold rolling effect on the mechanical behavior of TiNi SMAs has been recognized over several decades ago [44], the actual mechanism underlying such an effect has remained a mystery since then. Various hypotheses have been proposed in these previous studies, including combined effect of elastic deformation of nano-B2 grains and amorphous phase, and dominance of interfacial energy associated with the nanocrystals, etc. [45-48], but none of them is actually responsible for the unique mechanical behavior of the cold rolled alloys. As will be shown in this study, for example, in samples with relatively small amount of cold rolling (e.g., much smaller than 40%) without annealing, little nanocrystalline or amorphous structures exist [47], but they did exhibit the unique mechanical behavior.

In this paper, we report for the first time a B19′ strain glass state in NiTi by cold rolling (27%). Our experiments reveal unambiguously that the reason behind the

unique mechanical behavior is actually the B2 to B19' strain glass transition. Normal MTs are suppressed as indicated by the absence of obvious Differential Scanning Calorimetry (DSC) peaks. Frequency dispersion of storage modulus in the Dynamic Mechanical Analysis (DMA) measurements marks the appearance of strain glass transition. The continued decrease of electrical resistivity (ER) upon cooling and the gradual growth of B19′ nanodomains from in-situ Transmission Electron Microscope (TEM) observations confirm the B19′ strain glass state. Such a B19′ strain glass state is the physical origin of quasi-linear elasticity with large recovery strain over wide temperature.

Samples used in this study are purchased from SaiTe Company with composition ($Ni_{50.8}Ti_{49.2}$). The as-received samples are sealed in evacuated quartz tubes with Ar atmosphere and solution treated at temperature of 1173K for 24h followed by water quench to obtain a homogeneous solid solution. Then the samples are cold-rolled to achieve different amount of plastic deformation ε_p (thickness reduction). The MT behaviors as a function of ε_p are characterized by DSC of TA Q200, DMA of TA Q800 and TEM of JEM 2100F. An MTS tensile machine and a Nyilas extensometer are used to measure the mechanical properties.

Inset of Fig. 1(a) show the DSC results of $Ti_{49.2}Ni_{50.8}$ upon cooling for different ε_p (from 0% to 70%). With the increase of ε_p, the exothermic peaks become broader and weaker and disappear completely when $\varepsilon_p \geq 27\%$. The enthalpy or entropy change associated with the MT in the cold rolled samples is calculated from DSC results. As shown in Fig 1(a), the transition entropy (ΔS) decreases gradually and vanishes at ε_p = 27%, indicating the disappearance of first order MT. The detailed DSC results for ε_p = 27% are shown in Fig. 1(b). The in-situ XRD results shown in the inset of Fig. 1(b) indicate that the system maintains a B2 structure (on average) upon cooling and there is no obvious change in the degree of strain order, which agrees well with previous observations of strain glasses [21,22,29,49]. The XRD measurements obtain the signal of a mixture of nanodomains of different martensitic variants embedded in a B2 matrix and thus cannot distinguish the existence of B19′ nanostructure and shows a

B2 structure. Defects generated by cold rolling play an important role in the decrease and disappearance of the enthalpy of transformation. The local stresses associated with the defects generated by the cold rolling could alter the nature of the austenite (A) to martensite (M) transformation. As the stress level increases, the nature of the A to M transformation changes gradually from a strongly first-order to a weekly first-order and eventually to a high-order transition [50]. On the other hand, there exists a wide distribution of defect strength (i.e., the magnitude of local stresses associated with the defects), which leads to continuous nucleation and growth of martensitic domains upon cooling. The small amount of martensitic phase transformed at each temperature produces very weakly and even zero (if second-order in nature as mentioned above) heat release. At 27% cold rolling the defects generated seem to have the strength and strength distribution that change the transformation behavior and results in nearly zero transformation enthalpy.

To identify the origin of the vanishing transition entropy at $\varepsilon_p \geq 27\%$ in the DSC results, DMA is used to measure the viscoelasticity of the samples. As shown in Fig. 2, a gradual softening of storage modulus [38] is detected upon cooling for samples with $\varepsilon_p = 27\%$, 40% and 70%, which is different from the sharp modulus change associated with normal MT [38,49]. The dip temperatures of the storage modulus are obviously frequency-dependent and the experimental data follow closely the Vogel-Fulcher relation ($\omega = \omega_0 \times e^{-\frac{E_a}{K_B(T_g - T_0)}}$, where ω is the measuring frequency, E_a is the activation energy, K_B is the Boltzmann constant, T_g is the measured glass transition temperature at certain measuring frequency, and T_0 is the ideal glass transition temperature), indicating clearly a glass transition behavior [18,34].

To determine the crystal structures of the strain glass state (e.g., R or B19′ strain glass), electrical resistivity (ER) measurements are carried out by taking advantage of the sensitive and opposite dependence of the resistivity of the R and B19′ phases on temperature. From previous studies, we know that ER increases accompanying the B2 to R transition [51], while ER decreases accompanying the B2 to B19′ and R to B19′ transitions [21,49]. As shown in Fig. 2 (on the right axis), two extrema (i.e., local

minimum, $T_{\rho min}$, and local maximum, $T_{\rho max}$) appear in the temperature vs. relative ER curve of the samples with ε_p=27%. Within the temperature range between $T_{\rho min}$ and $T_{\rho max}$ the ER shows a slight increase upon cooling, which could correspond to the appearances and growth of R nanodomains. On the other hand, the gradual decrease of ER below $T_{\rho max}$ could indicate the appearance and growth of B19′ nanodomains. Thus, the storage modulus softening below T_g and the gradual decrease of ER below $T_{\rho max}$ in Fig. 2 are consistent, which suggests a strain glass transition with local B19′ structure.

Direct observations of the microstructures of the strain glass state at different temperatures are made using in-situ cooling TEM for the samples with ε_p = 27% in a temperature range between 298K and 96K. At 298K (RT), the diffraction pattern (Fig. 3a) shows diffuse scatterings concentrated near $1/2(011)_{B2}$ and $1/3(011)_{B2}$ along with primary B2 reflections. This indicates the co-existence of local R and B19′ structures in the matrix, while the average structure remains B2. The concentrated diffuse scatterings become stronger during cooling. More interesting observations come from the corresponding temperature-dependent in-situ dark field images (DFI) of the superreflections indicated in Figs. 3(a) - (d), which reveal nano-sized B19′ and R local regions below 10 nm. With decreasing temperature (Figs. 3(a′) - (d′)), the R-like nanodomains grow in size and numbers, but start disappearing below T_g, indicating transitions from B2 to R to B19′ at nanoscale. On the other hand, as shown in Figs. 3(a″) - (d″), the B19′ like nanodomains grow continuously during cooling till T_g below which these nanodomains are frozen without evolving into internally twined B19′ martensitic plates with long-range strain order (i.e., strain crystal).

Because of their drastically different transition characteristics (i.e., broadly smeared and continuous) as compared to that of MTs (sharp and discontinuous), strain glass systems have some unprecedented properties. As shown in Fig. 4 (a), the B19′ strain glass has a quasi-linear superelasticity with a large recoverable strain of ~ 4%, a small hysteresis and a high strength of ~1.0GPa over a wide temperature ~200K (from 323K to 123K). The tensile stress-strain curves were obtained at different

temperatures with a constant strain rate of $0.005min^{-1}$. The curves at different temperatures are shifted horizontally for a better display. Figure 4 (b) shows the size of the stress-strain hysteresis loops calculated by integrating the areas within the loops. All the hysteresis loops are rather small within the measured temperature range and decrease upon cooling. Figure 4(c) shows that the apparent elastic modulus (which is calculated by $E = \frac{\sigma_{0.2\%}}{0.2\%}$) will first decrease and then increase upon cooling which is consistent with the DMA results shown in Fig. 2. The change of the elastic modulus is related to the change of the amount of interfaces between martensite and austenite during the strain glass transition [38]. Note that all the stress-strain results are obtained after one pre-straining cycle to eliminate the unrecoverable strain at different temperatures. A load cycling test was carried out at room temperature to examine the functional fatigue behavior, as shown in Figure 4(d) and (e). A large open-loop strain was observed only at the first cycle. Then a stable strain state was reached after tens of cycles and large recoverable strain (~4%) remains after 30 cycles.

Structural glass describes a disordered arrangement of atoms, while strain glass describes a disordered arrangement of transformation strains. Strain glass is a conjugate state of strain crystal where the transformation strains are arranged with long-range order. Previous simulations have demonstrated the importance of defect strength [42] and elastic anisotropy (i.e., long range interaction) [43] on strain glass transitions. In the case of point defect doped TiNi SMAs, only the R strain glass state can be created due to the relatively small lattice distortion caused by the point defects. The current study suggests that defects of much higher strength (such as dislocations generated by cold rolling) become necessary to create a B19′ strain glass that has a much larger transformation strain.

Based on the above experimental observations (including the in-situ dark field image shown in Fig. 3), schematic drawings of microstructural evolution as well as the free energy curves for the two cases with $\varepsilon_p = 0\%$ and $\varepsilon_p = 27\%$ are made and shown in Fig. 5. In the solution treated samples without cold work (i.e., $\varepsilon_p = 0\%$), normal B2 to B19′ MT takes place and multiple martensitic variants arrange into a long-range

ordered twin structure upon cooling (Fig. 5 (a2)) and a de-twinned single domain structure upon loading (Fig. 5(a3)). During cold work, high densities of defects (e.g., dislocations) are generated [52]. The local stress fields associated with these defects will tilt the free energy landscape and either induce or suppress the formation of certain martensitic variants. When the amount of cold work exceeds a critical level (e.g., ε_p $\geq$27%), due to the confinement of densely populated extended defects, nanodomains of martensite with short-range strain order are stabilized at low temperatures and cannot evolve into long-range ordered strain domains (Fig. 5 (b1) and (b2)). Thus, in contrast to the normal internally twinned (i.e., long-range ordered) martensitic structure, a B19′ strain glass state, consisting of nanodomains of different B19′ martensitic variants randomly embedded in the B2 matrix (i.e., without any long-range correlations), is formed.

Thus, cold rolling creates a broad spectrum of defects that induce martensitic embryos with a broad spectrum of maturities and thus different local M_s for temperature-induced MT (see Fig. 5(b1) and b2)) or different critical stress for stress-induced MT at different locations (see Fig. 5(b3)). Defects with the highest potency will induce martensitic domains at the highest temperature, as shown in Fig. 5(b1), and the free energy curves of local regions with such defects are illustrated by the dark green and dark red curves in Fig. 5(b1). Because of the confinement from the surrounding regions where the potency of the defects is low and thus A is stable (see the free energy curve with light green and light red in Fig. 5(b1)), the martensitic domain size is limited to small size. Upon cooling, there will be continued formation and limited growth of "nano martensite" (see Fig. 5 (b2)).

During loading, certain martensitic domains favored by the local stresses of defects but unfavored by the external loading (green color) will shrink and disappear, while those favored by both internal defects and external load (red color) will grow, as shown in Fig. 5 (b3) and corresponding free energy curves in Fig. 5(b3′). Upon heating or unloading, the local stress fields associated with the defects that favor different martensitic variant at different locations will restore gradually the original

structural states without the need for nucleating new martensitic domains, leading to slim hysteresis.

In summary, the first B19′ strain glass is discovered in a cold rolled $Ti_{49.2}Ni_{50.8}$ system, which has shown mechanical properties including quasi-linear superelasticity with large recoverable strain (~4%) and slim hysteresis and high strength (~1GPa) over a wide temperature range (~200K). The defect structures generated by cold rolling induce B19′ martensitic embryos of widespread maturities that regulate the nucleation process of B19′ martensitic domains during both forward and backward transformations. In the meantime, the defects impose effectively nano-confinements that regulate the growth process of the B19′ martensitic domains (suppressing the autocatalysis effect). These combined effects convert a typically sharp, discontinuous first-order MT into a strain glass transition, which is responsible for all the unprecedented properties of the system.

Acknowledgements

The work was supported by the National Key Research and Development Program of China (Grants No. 2016YFB0701302, 2014CB644003) the National Natural Science Foundation of China (Grants No. 51671156, 51501145, 51431007 and 51231008), 51321003, IRT13034, 51621063 and the US National Science Foundation Grant No. DMR-1410322 and US Department of Energy Grant No. DE-SC0001258.

References:

[1] H. Walia, W. A. Brantley, and H. Gerstein, J. Endod. **14**, 346 (1988).
[2] D. E. Allie, C. J. Hebert, and C. M. Walker, Endovasc Today **7**, 22 (2004).
[3] P. D. L. Yahia, *Shape Memory Implants* (Springer Berlin Heidelberg, 2000).
[4] M. Kohl, *Shape Memory Microactuators* (Springer Science & Business Media, 2004).
[5] K. Otsuka and C. M. Wayman, *Shape memory materials* (Cambridge University Press, Cambridge ; New York, 1998).
[6] E. K. Salje, *Phase Transitions in Ferroelastic and Co-elastic Crystals* (Cambridge University Press, Cambridge, England, 1993).
[7] K. Otsuka and X. Ren, Prog. Mater. Sci. **50**, 511 (2005).
[8] J. Van Humbeeck, Adv. Eng. Mater. **3**, 837 (2001).

[9] J. K. Allafi, X. Ren, and G. Eggeler, Acta. Mater. **50**, 793 (2002).
[10] J. Khalil-Allafi, A. Dlouhy, and G. Eggeler, Acta. Mater. **50**, 4255 (2002).
[11] Y. Yang, S. Li, X. Ding, J. Sun, and E. K. Salje, Adv. Funct. Mater. **26**, 760 (2016).
[12] Z. Zhang, X. Ding, J. Sun, T. Suzuki, T. Lookman, K. Otsuka, and X. Ren, Phys. Rev. Lett. **111**, 145701 (2013).
[13] S. Hao, L. Cui, D. Jiang, X. Han, Y. Ren, J. Jiang, Y. Liu, Z. Liu, S. Mao, Y. Wang, Y. Li, X. Ren, X. Ding, S. Wang, C. Yu, X. Shi, M. Du, F. Yang, Y. Zheng, Z. Zhang, X. Li, D. E. Brown, and J. Li, Science **339**, 1191 (2013).
[14] W.-F. Rao and A. G. Khachaturyan, Acta. Mater. **59**, 4494 (2011).
[15] W.-F. Rao, M. Wuttig, and A. G. Khachaturyan, Phys. Rev. Lett. **106**, 105703 (2011).
[16] J. Cui, Y. S. Chu, O. O. Famodu, Y. Furuya, J. Hattrick-Simpers, R. D. James, A. Ludwig, S. Thienhaus, M. Wuttig, and Z. Zhang, Nat. Mater. **5**, 286 (2006).
[17] R. Zarnetta, R. Takahashi, M. L. Young, A. Savan, Y. Furuya, S. Thienhaus, B. Maaß, M. Rahim, J. Frenzel, and H. Brunken, Adv. Func. Mater. **20**, 1917 (2010).
[18] S. Sarkar, X. Ren, and K. Otsuka, Phys. Rev. Lett. **95**, 205702 (2005).
[19] D. Wang, Y. Z. Wang, Z. Zhang, and X. B. Ren, Phys Rev Lett **105**, 205702 (2010).
[20] L. Nguyen, D. Wang, Y. Wang, and M. De Graef, Acta. Mater. **94**, 172 (2015).
[21] D. Wang, Z. Zhang, J. Zhang, Y. Zhou, Y. Wang, X. Ding, Y. Wang, and X. Ren, Acta. Mater. **58**, 6206 (2010).
[22] Y. Zhou, D. Xue, X. Ding, Y. Wang, J. Zhang, Z. Zhang, D. Wang, K. Otsuka, J. Sun, and X. Ren, Acta. Mater. **58**, 5433 (2010).
[23] X. Ren, Appl. Phys. Lett. **95**, 151906 (2009).
[24] S. Semenovskaya and A. G. Khachaturyan, Acta. Mater. **45**, 4367 (1997).
[25] P. Lloveras, T. Castán, M. Porta, A. Planes, and A. Saxena, Phys. Rev. Lett. **100**, 165707 (2008).
[26] J. Liu, M. Jin, C. Ni, Y. Shen, G. Fan, Z. Wang, Y. Zhang, C. Li, Z. Liu, and X. Jin, Phys. Rev. B **84**, 140102 (2011).
[27] Y. Wang, J. Gao, H. Wu, S. Yang, X. Ding, D. Wang, X. Ren, Y. Wang, X. Song, and J. Gao, Sci Rep **4**, 3995 (2014).
[28] Y. Ji, X. Ding, T. Lookman, K. Otsuka, and X. Ren, Phys. Rev. B **87** (2013).
[29] J. Zhang, D. Xue, X. Cai, X. Ding, X. Ren, and J. Sun, Acta. Mater. **120**, 130 (2016).
[30] L. E. Cross, Ferroelectrics **76**, 241 (1987).
[31] B. Vugmeister and H. Rabitz, Phys. Rev. B **57**, 7581 (1998).
[32] G. A. Samara, J. Phys. Condens. Matter **15**, R367 (2003).
[33] D. Sherrington, Phys. Rev. Lett. **111**, 227601 (2013).
[34] M. JA, *Spin glasses* (Taylor & Francis, London, 1993).
[35] K. Binder and A. P. Young, Rev. Mod. Phys. **58**, 801 (1986).
[36] D. Sherrington and S. Kirkpatrick, Phys. Rev. Lett. **35**, 1792 (1975).
[37] D. Wang, S. Hou, Y. Wang, X. Ding, S. Ren, X. Ren, and Y. Wang, Acta. Mater. **66**, 349 (2014).

[38] L. Zhang, D. Wang, X. Ren, and Y. Wang, Sci Rep **5**, 11477 (2015).
[39] J. Cui and X. Ren, Appl. Phys. Lett. **105**, 061904 (2014).
[40] Z. Tang, Y. Wang, X. Liao, D. Wang, S. Yang, and X. Song, J. Alloys Compd. **622**, 622 (2015).
[41] Y. Nii, T. Arima, H. Y. Kim, and S. Miyazaki, Phys. Rev. B **82**, 214104 (2010).
[42] D. Wang, D. Lv, Y. Gao, Y. Wang, X. Ren, and Y. Wang, J. Alloys Compd. **661**, 100 (2016).
[43] P. Lloveras, T. Castán, M. Porta, A. Planes, and A. Saxena, Phys. Rev. B **81**, 214105 (2010).
[44] T. Tadaki and C. M. Wayman, Scr. Metal. **14**, 911 (1980).
[45] K. Tsuchiya, Y. Hada, T. Koyano, K. Nakajima, M. Ohnuma, T. Koike, Y. Todaka, and M. Umemoto, Scr. Mater. **60**, 749 (2009).
[46] H. Nakayama, K. Tsuchiya, and M. Umemoto, Scr. Mater. **44**, 1781 (2001).
[47] K. Tsuchiya, M. Inuzuka, D. Tomus, A. Hosokawa, H. Nakayama, K. Morii, Y. Todaka, and M. Umemoto, Mater. Sci. Eng., A **438-440**, 643 (2006).
[48] A. Ahadi and Q. Sun, Appl. Phys. Lett. **103**, 021902 (2013).
[49] Z. Zhang, Y. Wang, D. Wang, Y. Zhou, K. Otsuka, and X. Ren, Phys. Rev. B **81** (2010).
[50] F. Falk, JOURNAL DE PHYSIQUE **43**, c4 (1982).
[51] Y. Murakami and D. Shindo, Philos. Mag. Lett. **81**, 631 (2001).
[52] G. E. Dieter and D. J. Bacon, *Mechanical metallurgy* (McGraw-Hill, New York, 1986).

Figure Captions

Figure 1 (a) The change in entropy of transition for samples having different amounts of cold work ε_p, inset describes the DSC results with ε_p from 0% to 70% upon cooling. (b) DSC results with ε_p =27% show no obvious endothermic and exothermic peak, the inset shows in-situ XRD results indicating that the sample maintains a B2 structure upon cooling.

Figure 2 DMA measurements of frequency-dependence of storage modulus (left axis) upon cooling for $Ti_{49.2}Ni_{50.8}$ with ε_p = 27% (a), ε_p = 40% (b) and ε_p = 70% (c). The inset shows the Vogel-Fulcher fitting results of T_g (storage modulus dip temperature) and T_0 is the ideal glass frozen temperature. The normalized (at 298K) electrical resistivity curves (for cooling) of $Ti_{49.2}Ni_{50.8}$ with ε_p = 27% are also shown in (a) (right axis). The arrows indicate temperatures at which the electrical resistivity reaches the extremum points, i.e., local minimum ($T_{\rho min}$) and local maximum ($T_{\rho max}$), respectively.

Figure 3 TEM dark-field images and the corresponding diffraction patterns of $Ti_{49.2}Ni_{50.8}$ cold-rolled down to a thickness reduction of 27%: (a), (a′) and (a″) at T=298 K > T_g; (b), (b′) and (b″) at T=243K ~ T_g; (c), (c′) and (c″) at T=193K < T_g; (d), (d′) and (d″) at T=96K. The zone axis is $[111]_{B2}$.

Figure 4 (a) Stress-Strain curves at different temperatures, which were performed under tensile test with strain control . The curves of different temperature are shown horizontally for a better exhibition. (b) Temperature dependence of stress hysteresis. (c) temperature dependence of elastic modulus obtained at different temperatures for $Ti_{49.2}Ni_{50.8}$ with ε_p=27%. (d) 30 times tensile Cycling test isothermally at room temperature for $Ti_{49.2}Ni_{50.8}$ with ε_p=27%; and (e) the evolution of maximum strain and

residual strain under cycling test.

Figure 5 Schematic drawing of microstructure evolution and the associated free energy curves at ε_p=0 (a1- a3′) and at ε_p=27% (b1 – b3′) upon cooling and loading. (a1) and (a1′), microstructure and free energy curve at high temperature (HT) where the austenite is stable. (a2) and (a2′), microstructure and free energy curve at low temperature (LT) where martensite (both variants M1 and M2) is stable. (a3) and (a3′), microstructure and free energy curve under loading where a single martensitic variant (M2) is stable. (b1) and (b1′), microstructure and free energy curve at high temperature (HT) with randomly distributed martensitic domains (small volume fraction). (b2) and (b2′), microstructure and free energy curve at high temperature (LT) with randomly distributed martensitic domains (large volume fraction). (b3) and (b3′), microstructure and free energy curve under loading with the external load favoring one of the martensitic variants. Free energy curves with different colors describe different local regions experiencing different stresses. The green and red arrows in (b1′) through (b3′) indicate an increase in the local stress.

Figure 1

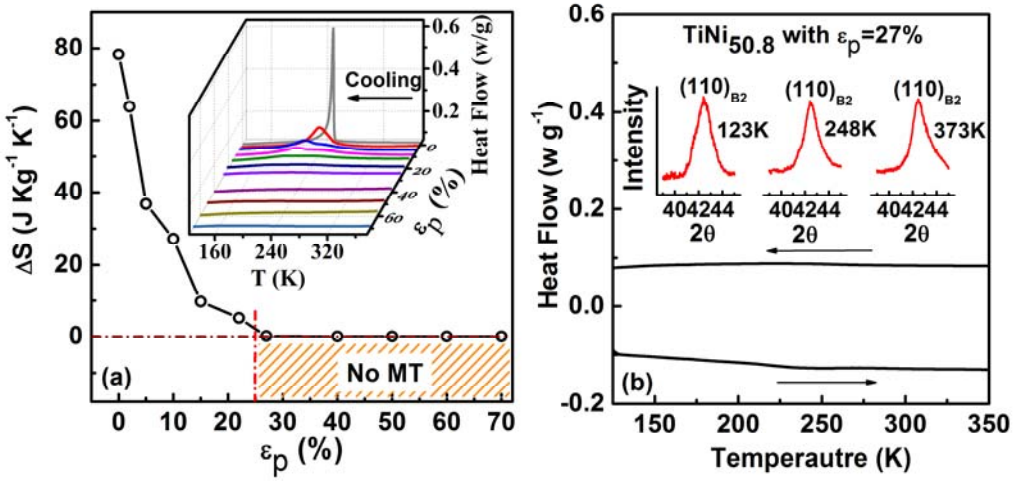
ΔS (J Kg-1 K-1)
εp (%)
No MT
(a)
Cooling
Heat Flow (w/g)
T (K)
TiNi50.8 with εp=27%
(110)B2
123K
248K
373K
Intensity
2θ
Heat Flow (w g-1)
Temperautre (K)
(b)

Figure 2

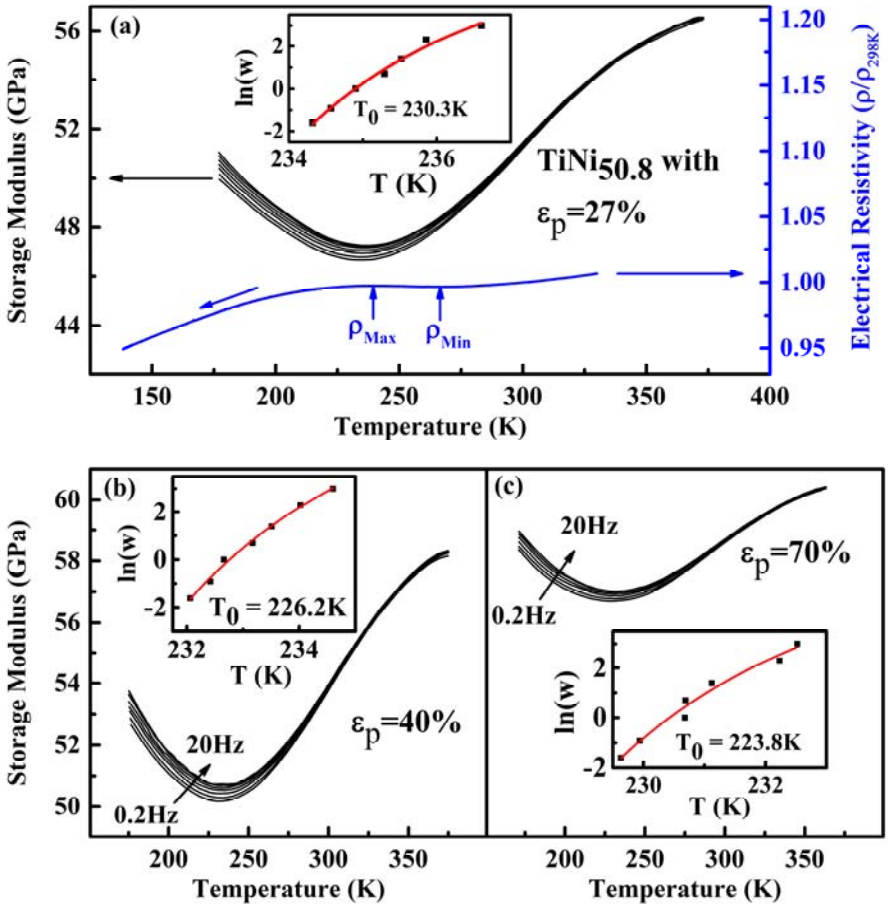
(a)
Storage Modulus (GPa)
Electrical Resistivity (ρ/ρ298K)
Temperature (K)
ln(w)
T0 = 230.3K
T (K)
TiNi50.8 with
εp=27%
ρMax
ρMin
(b)
T0 = 226.2K
20Hz
0.2Hz
εp=40%
(c)
εp=70%
T0 = 223.8K

Figure 3

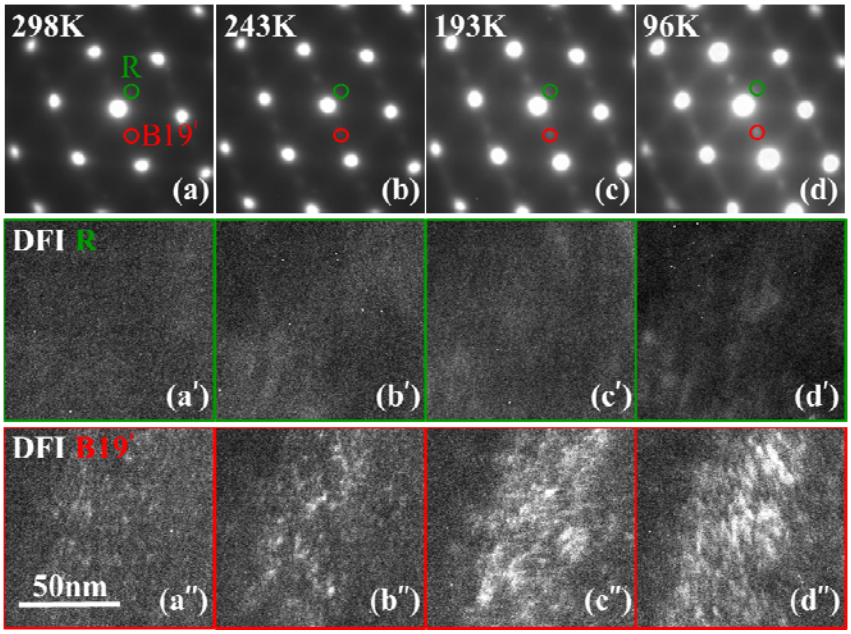

Figure 4

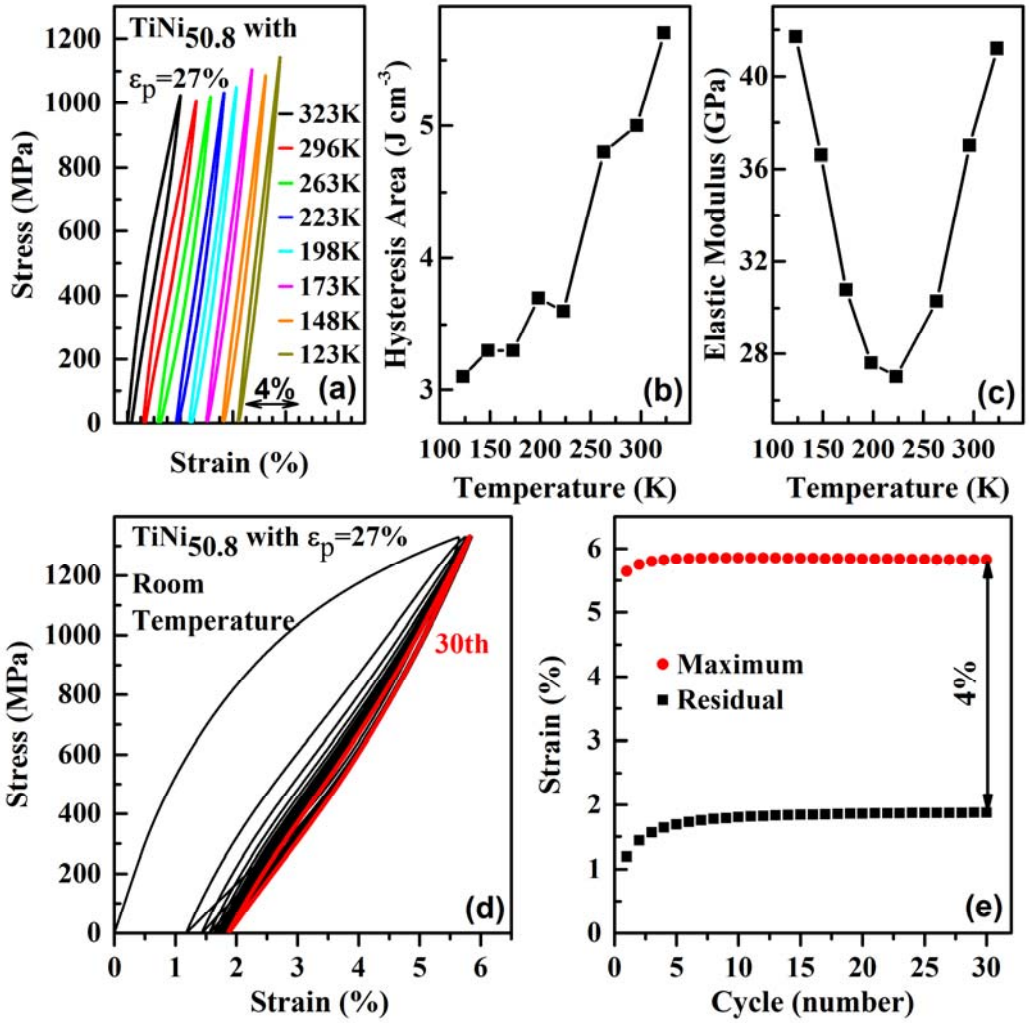
TiNi50.8 with
εp=27%
323K
296K
263K
223K
198K
173K
148K
123K
4%
(a)
Stress (MPa)
Strain (%)
Hysteresis Area (J cm-3)
(b)
Temperature (K)
Elastic Modulus (GPa)
(c)
Temperature (K)
TiNi50.8 with εp=27%
Room
Temperature
30th
(d)
Stress (MPa)
Strain (%)
Maximum
Residual
4%
(e)
Strain (%)
Cycle (number)

Figure 5

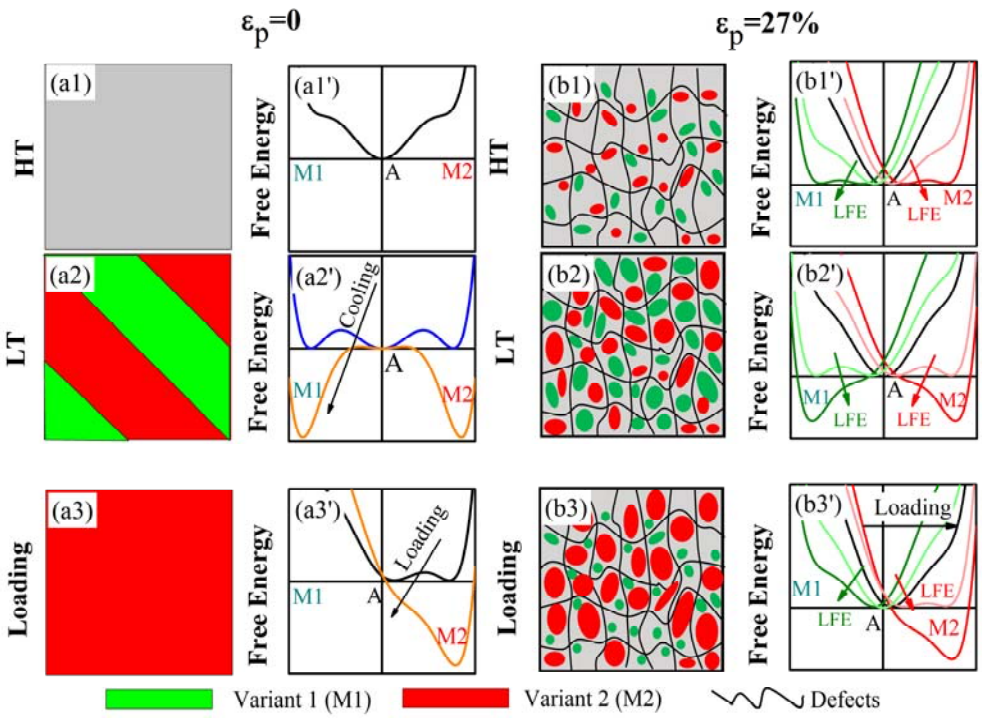
εp=0
εp=27%
HT
LT
Loading
(a1)
(a1')
(a2)
(a2')
(a3)
(a3')
(b1)
(b1')
(b2)
(b2')
(b3)
(b3')
Free Energy
M1
A
M2
Cooling
Loading
LFE
Variant 1 (M1)
Variant 2 (M2)
Defects